Materials Characterization 144 (2018) 99–112

Contents lists available at ScienceDirect

Materials Characterization

journal homepage: www.elsevier.com/locate/matchar

Correlation between corrosion resistance, anodic hydrogen evolution and microhardness in friction stir weldment of AA2198 alloy

Uyime Donatus[a,*], Barbara Victoria Gonçalves de Viveiros[a], Maicon Cavalieri de Alencar[a], Raphael Oliveira Ferreira[b], Mariana Xavier Milagre[a], Isolda Costa[a]

[a] Instituto de Pesquisas Energéticas e Nucleares, Av. Prof. Lineu Prestes, 2242 São Paulo,Brazil
[b] Escola Politécnica da Universidade de São Paulo, Av. Professor Mello Moraes, 2463 São Paulo, SP, Brazil

ARTICLE INFO

Keywords:
Aluminium alloy
Friction stir welding
Pitting corrosion
Anodic hydrogen evolution

ABSTRACT

Correlation between corrosion resistance, anodic hydrogen evolution and microhardness in the friction stir weldment of AA2198-T851 alloy has been investigated. Different microscopy techniques, scanning vibrating electrode technique (SVET) and potentiodynamic polarization tests were employed in the investigation. Unlike other 3rd generation Al-Cu-Li alloys where the regions that are most susceptible to corrosion are always within the weld region, the results reveal that the parent material is the most susceptible in this case. There is a direct correlation between corrosion resistance, anodic hydrogen evolution and microhardness in the weldment, and the T_1 phase is associated with the direct correlation.

1. Introduction

New generation Al-Cu-Li alloys, in which the AA2198-T851 is a representative member, have been developed primarily for aerospace applications [1]. The properties of these alloys have been reported to be very promising [1,2]. However, the understanding of the structure – property – performance relationships of these alloys is far from being complete [1,2], and this includes the weldments of these alloys. Unarguably, friction stir welding has become a very important welding process for Al alloys. Thus, it is necessary to understand the mechanical and corrosion behaviours of the weldments of the new (3rd) generation Al-Cu-Li alloys such as that of the AA2198-T851 alloy.

Most age hardenable Al alloys typically exhibit a 'W' shape microhardness or hardness profile across the surface of their friction stir weldments [3]. The highest hardness values are usually recorded in the peak aged or near peak aged parent materials (PMs). The values decrease in the heat affected zone (HAZ) due to increasing coarsening and dissolution of the strengthening precipitates. The decrease in hardness values continues until the boundary between the HAZ and the thermomechanically affected zone (TMAZ) is reached [4]. In the nugget or stir zone (SZ), where dynamic recrystallization has occurred, the hardness values can either be lower or slightly higher than that of the adjacent TMAZ, and the HAZ closest to the TMAZ. This is dependent on the precipitation sequence of the alloy and or contribution of the grain boundaries to dislocation movement. Examples of the shape of the microhardness profile explained can be found in references [3–9]. In essence, the hardness profile across a peak aged or near peak aged heat treatable Al alloy friction stir weldment is somewhat predictable.

In contrast, the corrosion behaviour of the friction stir weldments of Al alloys is complex. Unlike in other alloy systems, the regions that are most susceptible to corrosion can be very different. Variations in the temper designation of an alloy or welding parameters can significantly affect the corrosion behaviour of the alloy [5,10–12]. A typical case of the effect of welding parameters on corrosion susceptibility can be found in the work of Jariyaboon and co-workers [5]. It was shown that for AA2024-T351 weldments produced with low rotation speeds, the attack was located mainly in the nugget; but for weldments produced at high rotation speeds, the attack was located mainly in the HAZ. Similarly, Esmaily and co-workers [12] showed that by increasing the number of friction stir processing passes for an extruded 6005-T6 alloy weldment, the extent of pitting corrosion in the nugget reduced and significant pitting corrosion was induced in the HAZ. Outside of welding parameters, different regions that are most susceptible to corrosion have been reported for different Al alloy weldments [8,13–18]. Thus, it is difficult to predict the region most susceptible to corrosion in friction stir weldments of Al alloys. Nonetheless, it is important to mention that the HAZ, TMAZ and SZ are usually reported to be the most susceptible regions, and rarely the PM of the weldments.

The complexity of the corrosion behaviour of friction stir weldments Al alloys is also true for the new generation Al-Cu-Li alloys. For an

* Corresponding author.
E-mail address: uyimedonatus@yahoo.com (U. Donatus).

https://doi.org/10.1016/j.matchar.2018.07.004
Received 19 June 2018; Received in revised form 2 July 2018; Accepted 6 July 2018
Available online 07 July 2018

Table 1
Chemical composition (wt%) of the AA2198-T851 Al-Cu-Li alloy employed in this study.

Elements	Cu	Mg	Si	Fe	Zn	Li	Zr	Ag	Al
Weight %	3.31	0.31	0.03	0.04	0.01	0.96	0.4	0.25	Balance

AA2050 friction stir weldment, without post weld heat treatment [16,19,20], the HAZ and SZ were reported to be anodic to the other regions of the weldment. Whereas, a recent study on the corrosion behaviour of 2A97 Al-Cu-Li friction stir weldment [13] revealed that the TMAZ of the weldment was the most susceptible region to corrosion. Interestingly, the T_1 phase, which is the primary strengthening phase, was attributed to the corrosion susceptibilities of the regions reported in both studies, and no direct correlation between the corrosion susceptibilities and variations in microhardness across the weldments were reported. In this study, the T_1 phase is also associated with the corrosion susceptibility. However, the most susceptible region to corrosion is different from the regions reported for the AA2050 and 2A97 Al-Cu-Li weldments. Furthermore, the correlation between the density of the T_1 phase, microhardness and corrosion susceptibility is also included in this study. In 2011, Bousquet and co-workers [14] carried out a similar investigation but on friction stir weldment of AA2024-T3 Al-Cu-Mg alloy. In their work, they clearly showed that there was no link between microhardness and corrosion sensitivity. This is because the microhardness of the investigated AA2024-T3 alloy is associated with the volume fraction of Guinier Preston Bagaryatski (GPB) zones and intragranular S'(S) precipitates. Whereas the corrosion sensitivity is associated with the size and density of coarse intermetallic compounds and on intergranular precipitation. The case of the AA2198-T851 alloy is different because both corrosion sensitivity and microhardness are associated with intragranular precipitation of T_1 particles. Thus, it is worth investigating the correlation between the microhardness, corrosion resistance and T_1 precipitation across the friction stir weldment of the alloy.

In addition, anodic hydrogen evolution (also termed negative difference effect) on Al alloys has been a topic of interest in recent times. Various attempts have been made to establish the understanding of the anodic hydrogen evolution mechanism, but the understanding is not yet fully understood [21,22]. Given that anodic hydrogen evolution has a strong relationship with the extent of corrosion susceptibility in Al

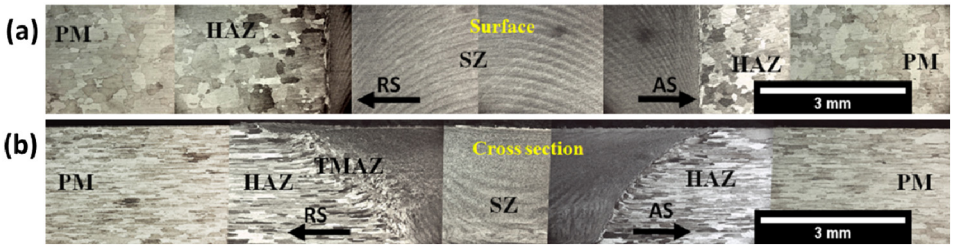

Fig. 1. Optical micrographs of the (a) surface and (b) cross-section of the friction stir weldment of AA2198-T851 alloy showing variations in grain sizes and grain morphologies in different zones of the weldment.

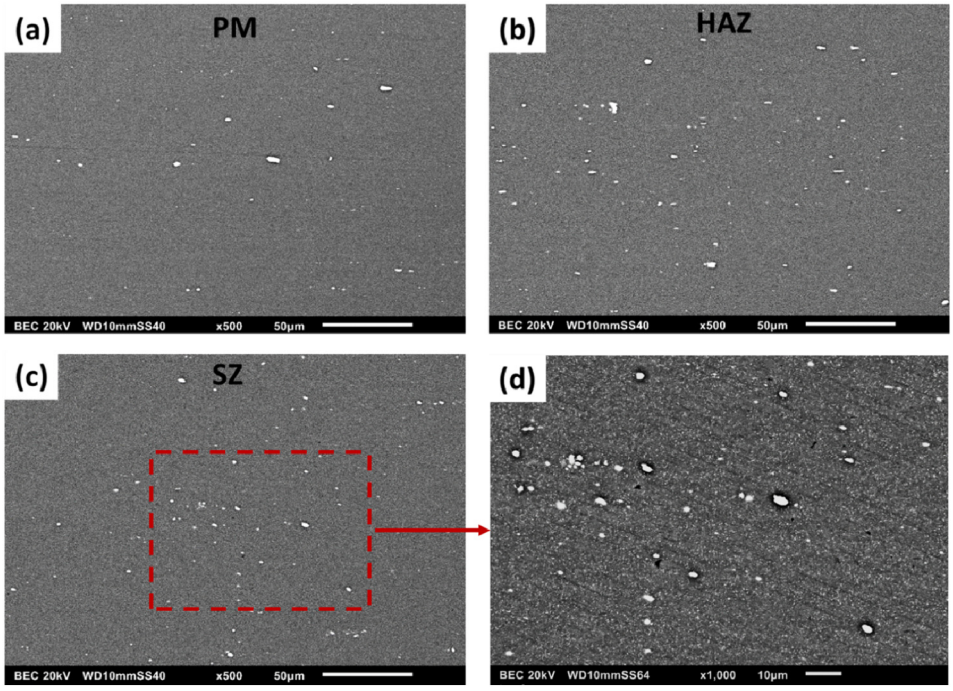

Fig. 2. SEM micrographs showing particle distribution in the (a) PM, (b) HAZ, ((c)–(d)) SZ of the AA2198-T851 alloy friction stir weldment.

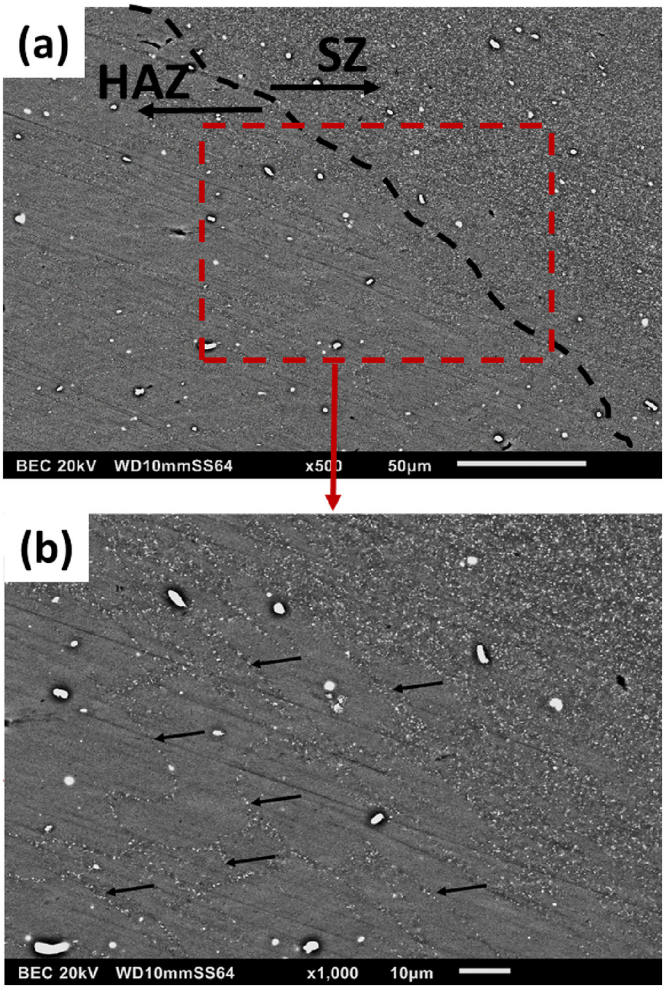

Fig. 3. SEM micrographs showing particle distribution in the transition region between the TMAZ and the SZ of AA2198-T851 friction stir weldment.

alloys, an attempt has also been made to qualitatively correlate this phenomenon with the microhardness and corrosion susceptibility of the AA2198-T851 friction stir weldment.

2. Experimental Procedure

Friction stir weldment of AA2198-T851 alloy was employed in this study. The composition of the alloy was obtained using inductively coupled plasma optical emission spectroscopy (ICP-OES) and it is given in Table 1. The welding was carried out using a tool with a shoulder diameter of 6 mm and a pin diameter of 2 mm. A rotation speed of 800 rpm and traverse speed of 150 mm/min was used for the welding.

Samples from the weldment were sequentially ground and polished to a 1 μm surface finish before any test or examination. For particle distribution examination under the scanning electron microscope (SEM), following polishing, samples were not subjected to further treatment after being rinsed, degreased and air cooled. Samples used to reveal grain sizes and morphologies were etched for 10 s using a solution comprising 2% hydrofluoric and 25% nitric acid. Transmission electron microscopy samples were prepared by twin-jet electropolishing technique with a solution comprising 35% HNO_3 in methanol, at −20 °C. Prior to twin-jet electropolishing, the thicknesses of the samples were reduced to 100 μm range by grinding and polishing.

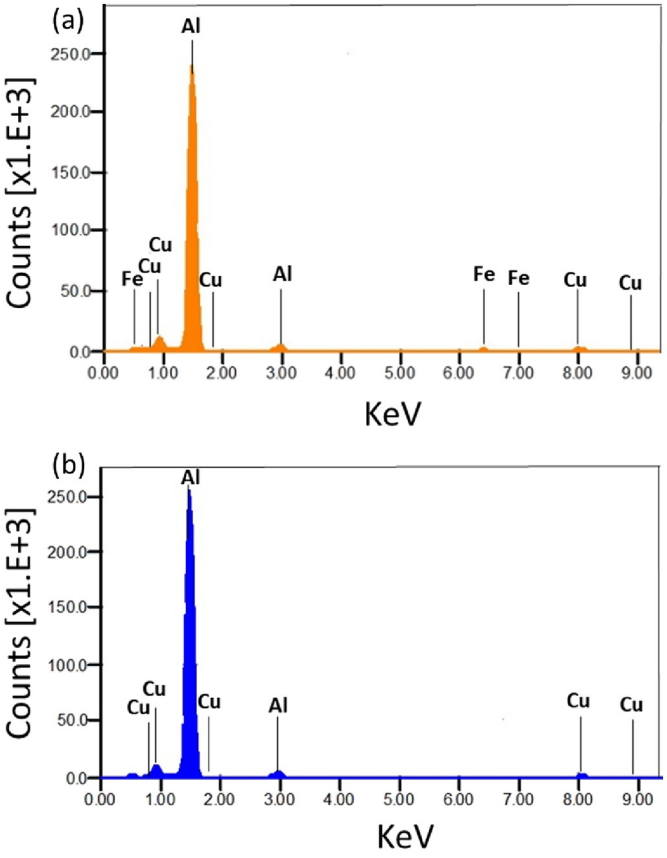

Fig. 4. Typical EDX profiles of the (a) Cu-Fe rich particles and (b) TB particles in the TMAZ and SZ of the AA2198-T851 friction stir weldment.

Following this, 3 mm diameter discs were cut from the samples for twin-jet electropolishing.

Vickers microhardness test was conducted using a load of 0.3 kg for a dwell time of 10 s for each measurement. Three sets of measurements were recorded across the polished surface of the weldment from the PM of the advancing side to the PM of the retreating side at an interval of 1 mm.

Scanning vibrating electrode technique (SVET) test was conducted in 0.01 mol L^{-1} NaCl solution for 26 h. An Applicable Electronics manufactured SVET machine was used for the test. A Pt-Ir probe was used for the test and the scan height was set at 100 μm. For the x-axis, the frequency was 174 Hz at an amplitude of 19 μm; while for the y-axis, the frequency was 73 Hz at the same vibrating amplitude. The capacitance of the probe before the commencement of the test was 2 nF. The scan step interval was 200 μm for a dwell time of 10 ms between successive scans. Scans were conducted every hour for up to 26 h.

In addition to the SVET test, immersion tests were also carried out for 24 h in exfoliation corrosion (EXCO) solution, 3.5% NaCl solution and acidified 3.5% NaCl solution (designated as A-3.5% NaCl solution). The EXCO solution was composed of 4 M NaCl, 0.5 M KNO_3 and 0.1 M HNO_3 in 1 L of deionised water, while the A-3.5% NaCl solution was prepared by adding 10 mL of HCl (35%) in 1 L of 3.5% NaCl solution. Samples subjected to immersion tests were immediately and thoroughly rinsed in deionised water and dried in a cool air stream before further examination.

Potentiodynamic polarization tests were conducted in the EXCO and A-3.5% NaCl solutions using a three-electrode set up comprising a Ag/AgCl (saturated KCl) reference electrode and a platinum counter

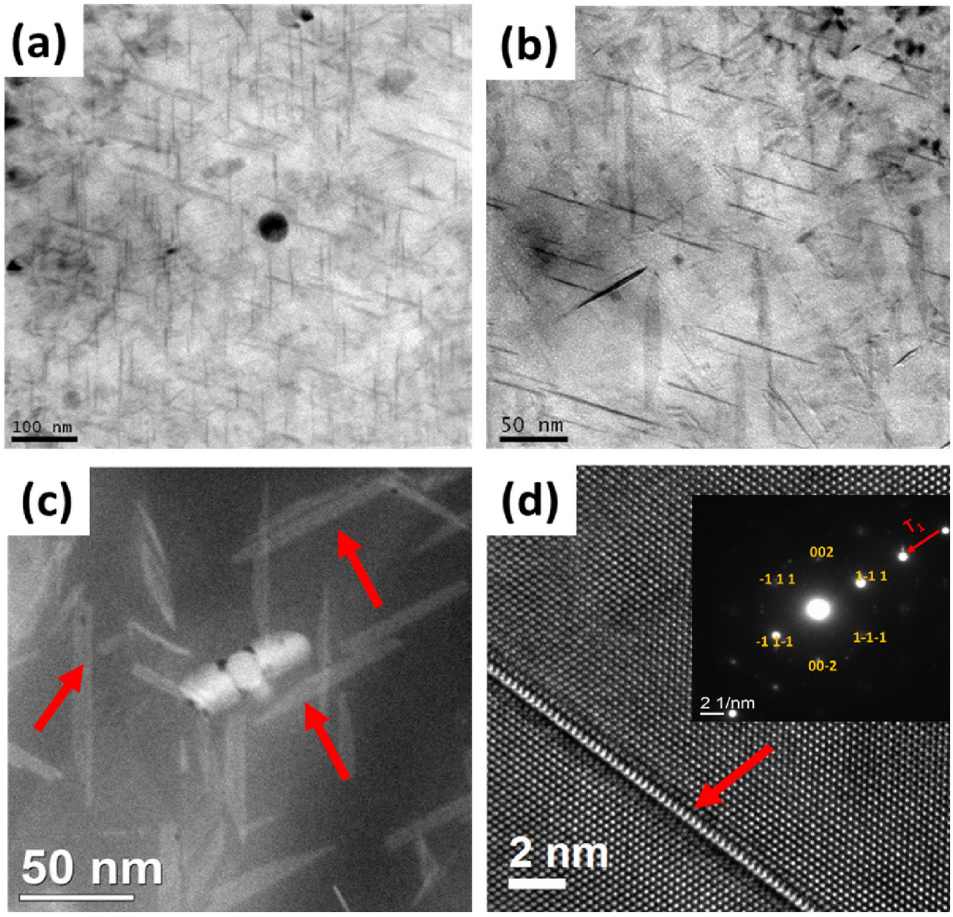

Fig. 5. TEM analysis of the PM: (a)–(b) bright field TEM micrographs and (c) HAADF image (d) HRTEM and SAED pattern image near [101] zone axis.

electrode. A cell designed to expose 0.025 cm^2 was employed for the polarization tests.

A Leica DMLM coupled optical microscope was employed for optical microscopy. Scanning electron microscopy was carried out using a JEOL JSM 6010LA SEM machine with acceleration voltage between 0.5 and 30 kV. The machine is also equipped with an energy dispersive X-ray spectroscopy (EDS) detector. SEM images were obtained in secondary and backscattered electron modes. A JEOL JEM 2100 transmission electron microscope (TEM) operating at 200 kV was also employed for microstructural analysis. Scanning transmission electron microscope (STEM) images were obtained using bright field and high angle annular dark field (HAADF) detector.

3. Results and Discussion

3.1. Microstructure and Microhardness

Presented in Fig. 1 are the optical micrographs of the surface (a) and cross-section (b) of the weldment showing the variations in grain sizes and morphologies across the weld zones.

The PM and HAZ of the AA2198-T851 alloy exhibited recrystallized equiaxed grains at the surface and elongated grains (beneath the near surface) in the direction of working. The TMAZ region in the retreating side spreads into the tool domain as observed from the cross-sectional micrograph, and it is difficult to clearly separate the severely fragmented grains of the TMAZ in the tool domain from the dynamically recrystallized grains of the SZ or nugget. For this reason, the SZ, in this case, represents the major part of the nugget (comprising very fine dynamically recrystallized grains) and a little of the TMAZ (comprising fragmented grains of the PM that have undergone extended recovery.

Figs. 2 and 3 present SEM micrographs showing the distribution of coarse second phase particles in the individual zones of the weld. As often reported, the distribution of the coarse second particles (brighter spots) is the same in the PM (Fig. 2(a)) and HAZ (Fig. 2(b)). These particles are mainly Cu-Fe rich intermetallic particles. A typical EDX profile for these types of particles is displayed in Fig. 4(a). No other kind of coarse intermetallic particle was observed, except for a few ones that contain little proportion of Si. These particles are fragmented and better distributed in the SZ (Fig. 2(c)). The Cu-Fe particles are not particularly affected by the heat generated from the welding process. With respect to corrosion, the Cu-Fe constituent particles are generally cathodic to the Al matrix. These particles are not associated with severe localized corrosion (SLC) in this alloy, they are associated with the formation of trenches and cavities [23].

Interestingly, a different type of second phase particle was observed to have precipitated at the grain boundaries in the HAZ and TMAZ of the weld and had precipitated uniformly across the entire SZ. This is displayed in Fig. 3(a) and (b). These particles are significantly finer than the Cu-Fe particles, as evident from the micrographs. EDS analysis of the particles, as shown in Fig. 4(b), revealed that the particles are Cu-rich particles. These precipitates are most likely T_B (Al_7Cu_4Li) particles [4,20]. In the study of precipitation in 2195 Al-Cu-Li alloy friction stir weld, Fonda and Bingert [4] reported that the T_B precipitates predominated in the SZ. Likewise, Chen and Chaturvedi [24] showed that

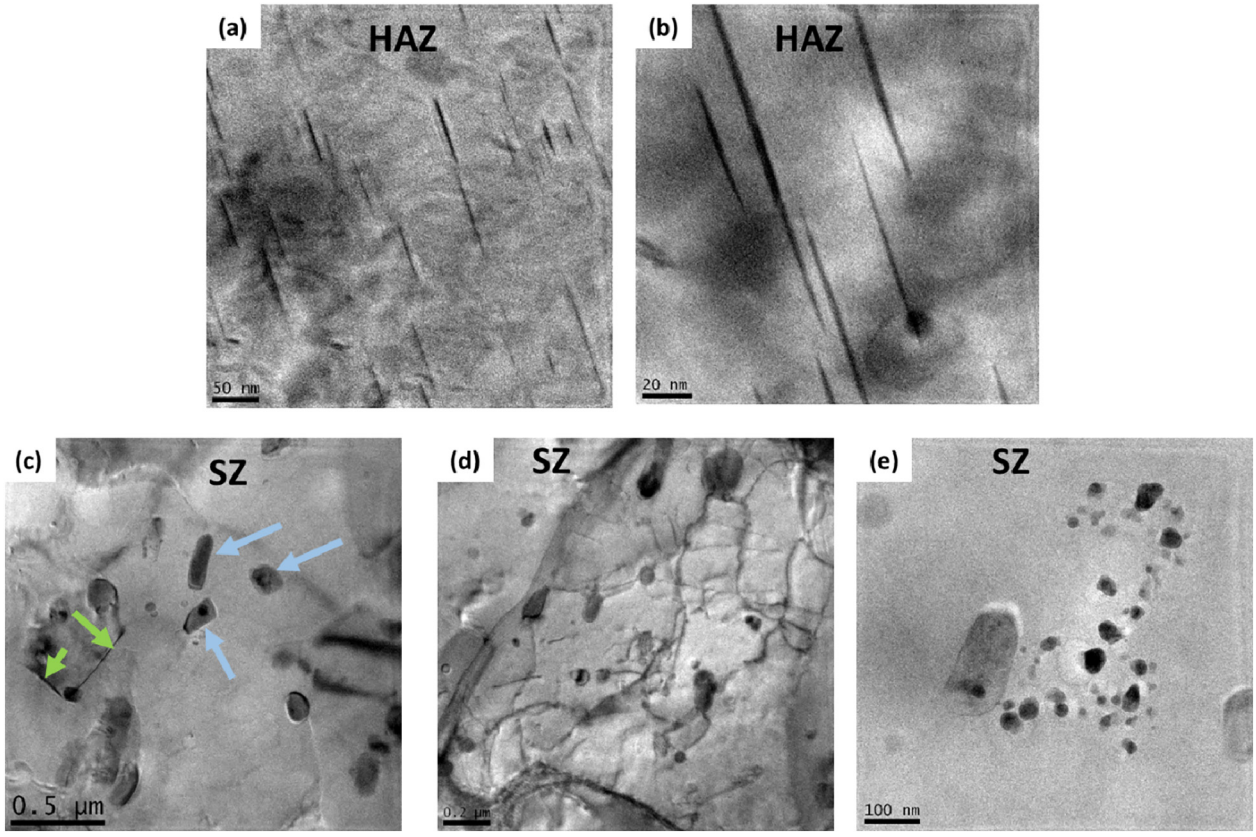

Fig. 6. TEM micrographs of the ((a)–(b)) HAZ and ((c)–(e)) SZ of the AA2198-T851 friction stir weldment.

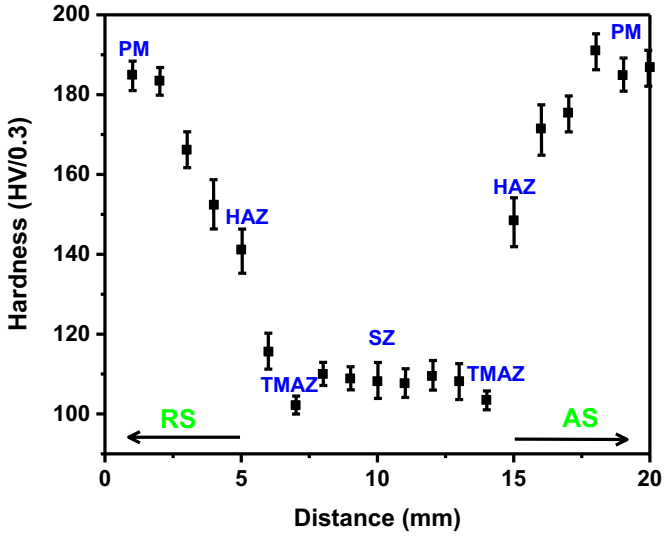

Fig. 7. Vickers microhardness trace from the PM in the RS to the PM in the AS across the surface of the AA2198-T851 friction stir weldment.

the T_B precipitates form along the grain boundaries of simulated HAZs of a 2195-T8 Al-Cu-Li alloy weld.

TEM micrographs obtained from different weld zones are displayed in Figs. 5–6. Various types of nano-sized precipitates were found in the PM side of the weldment (Fig. 5). However, the bright field TEM images (Fig. 5(a)–(b)) and the HAADF image (Fig. 5(c)) revealed that the T_1 phase (as indicated by the red arrows) is the most predominant phase in the PM. The analyses of the lattice fringe image and the selected area diffraction (SAED) pattern image in Fig. 5(d) confirm that this phase was the T_1 phase. The T_1 phase is the most important phase in terms of microhardness and resistance to severe localized corrosion. Displayed in Fig. 6(a)–(b) are the TEM micrographs of the HAZ of the weld. The images revealed that there is T_1 phase in the HAZ. However, the coarsening of the T_1 precipitates could have occurred due to the high temperature reached at this region. Further, the bright field images of the SZ, in Fig. 6(c)–(e), revealed no presence of the T_1 phase. The observable features were: dispersoids ((most likely Mn containing dispersoids) as indicated by the blue arrows in Fig. 6(c)); a phase appearing more like a Cu-containing phase of the S-type or θ-type (indicated by the green arrows in Fig. 6(c)); dislocations (Fig. 6(b)); and clusters of particles with shapes typical of the δ′/β′ precipitates [4,25] (Fig. 6(e)). The term δ′/β′ is being used for precipitates of the Al_3Li and Al_3Zr as both precipitates have similar morphologies and diffraction signatures [4]. In addition, they also exist together as composites with β′ (Al_3Zr) in the inner part and δ′ (Al_3Li) in the outer shell [25]. Evidently, the strengthening T_1 precipitates decreased in volume as the weld centre is approached, and dissolved completely in the SZ where the peak temperature is highest. These observations are supported by the works of Geuser and co-workers [26], who reported that there was a complete dissolution of the pre-existing T_1 precipitates in the weld nugget. Fonda and Bingert [4] also reported similar findings.

Fig. 7 displays the Vickers microhardness profile across the surface of the weldment. The typical 'W' shaped hardness profile is revealed. The microhardness values decreased from the PM (with microhardness values of 190 HV/0.3) across the HAZ (with significant variation in microhardness values) and TMAZ to the SZ (with microhardness values in the range 110 HV/0.3). The least microhardness values were

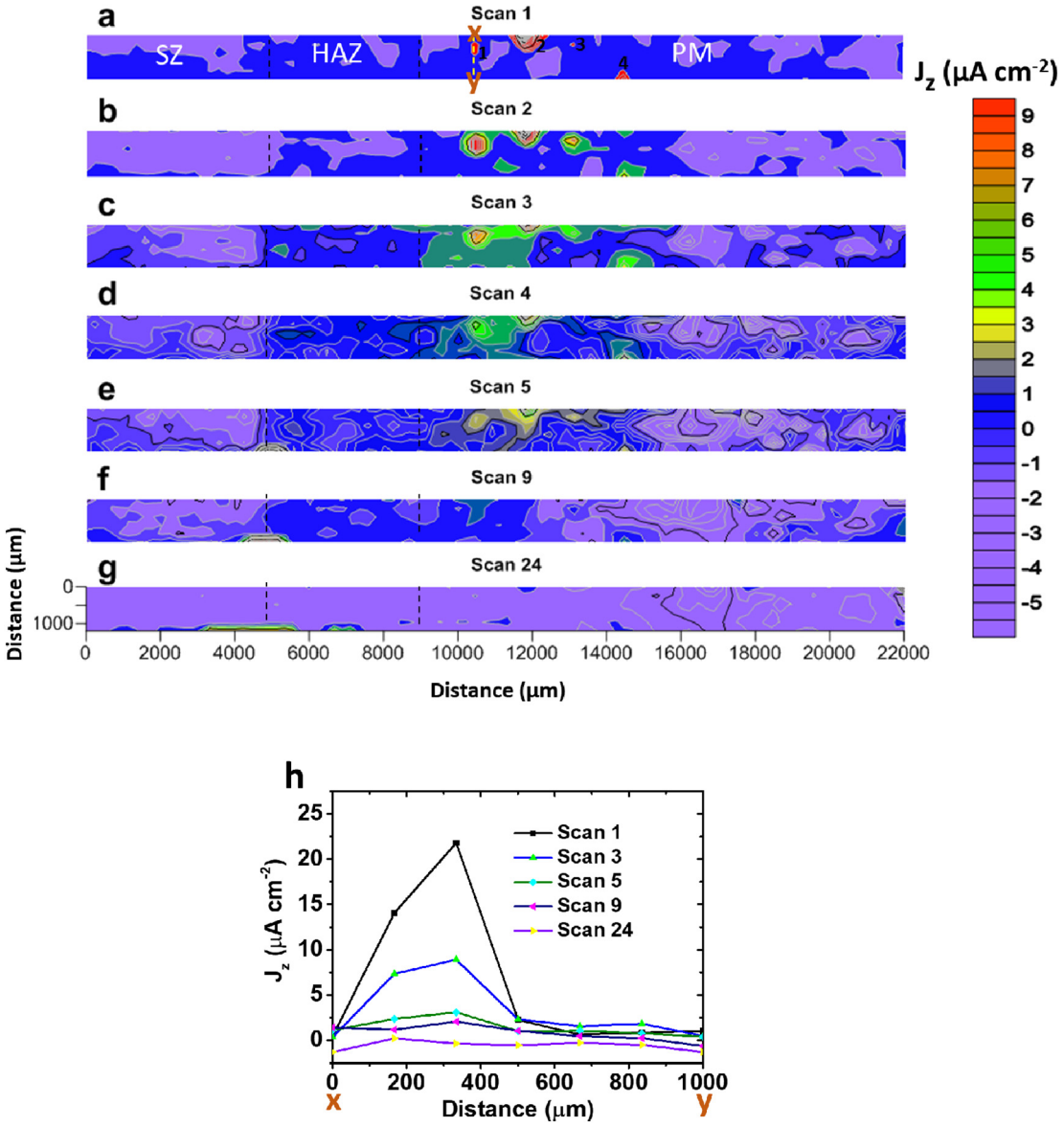

Fig. 8. (a)–(g) SVET maps of the surface of the AA2198-T851 weldment during immersion test in 0.01 mol L^{-1}. (h) Plot of current density values obtained for scans 1,3,5,9 and 24 across line xy as designated in (a). The scan numbers in the plots represent the hour after which the scan was obtained.

recorded at the boundary between the HAZ and the TMAZ. The variation in microhardness values from zone to zone correlates well with the changes in the amount of the T_1 phase, as discussed in the paragraph above. This is not surprising since the T_1 phase is the major strengthening precipitate in this alloy, and for the temper used in this study. In addition, works detailing the mechanical behaviour of peak/near peak aged Al-Cu-Li weldments also show this sort of relationship between the volume fraction of T_1 phase and microhardness variations [4,26–28].

3.2. Corrosion Susceptibility

SVET current density maps obtained during the immersion test of the weldment in 0.1 mol L^{-1} NaCl solution are displayed in Fig. 8(a)–(g). Fig. 8(h) displays the plot of current density values, obtained across line XY over the region designated as 1, for selected scans. From the current density maps, corrosion attack started within 1 h of exposure to the electrolyte. The areas that underwent severe localized corrosion are labelled as points 1, 2, 3 and 4 in Fig. 8(a). Optical micrographs confirming the severe localized corrosion that occurred at points 1, 2, and 3 are displayed in Fig. 9. All the severe localized corrosion areas were found in the PM region of the weldment. This shows that the PM region of the AA2198-T851 weldment is the most susceptible region to corrosion. The SVET maps show that, on the average, the current density values were relatively higher in the HAZ compared with the SZ. Thus, the SZ of the weldment was the most resistant region to corrosion in this medium. However, it must be stated that over time, the current density values evened out across the entire surface of the weldment. This is reflected in the map obtained after 24 h as shown in Fig. 8(g). Also, the line plots, in Fig. 8(h), confirms this. The line plot of scan 1 shows a peak current density value of about 22 μA cm^{-2} over area 1. After 3 h (scan 3), the peak current density value reduced significantly to values in the range of 9 μA cm^{-2}. Over time, the peak current density value decreased continuously until the current density values, over area 1, was about the same as the rest of the area along the

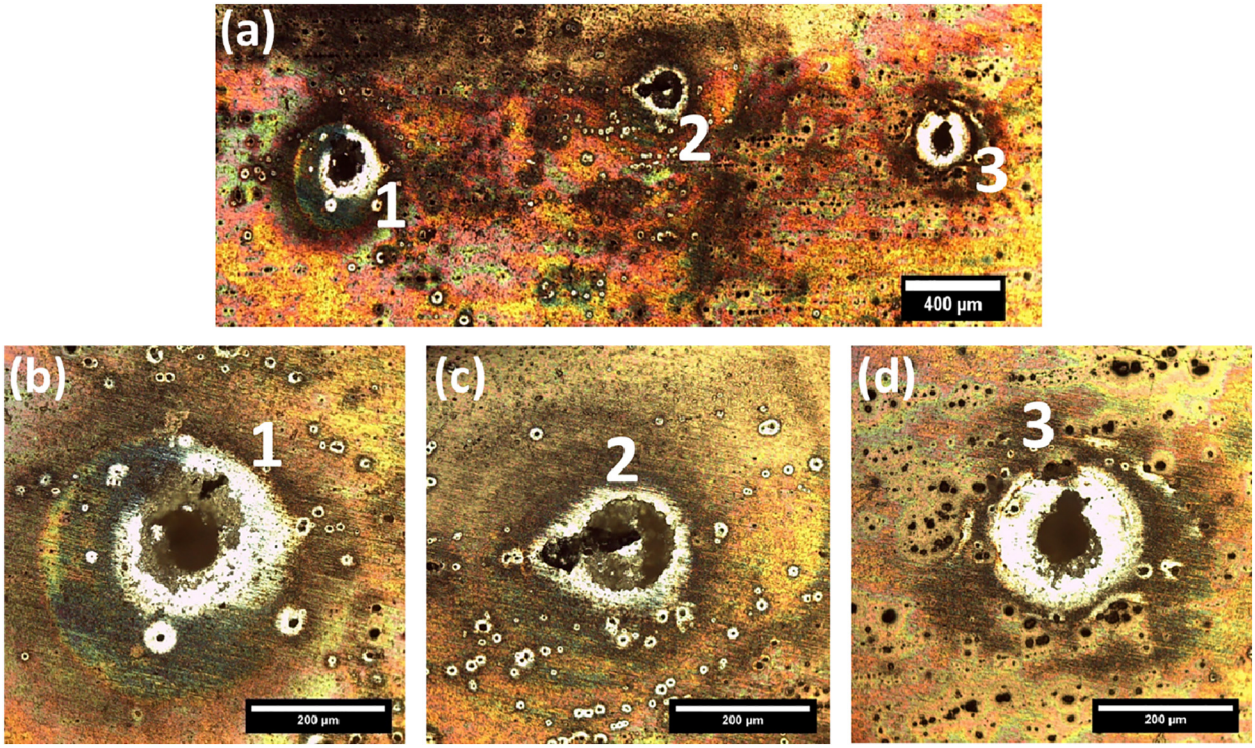

Fig. 9. Optical micrographs of the severe localized corrosion sites labelled 1, 2 and 3.

line XY. The current density decrease was as a result of the formation of voluminous corrosion products over the pit in area 1. Oxide/hydroxide or chloride containing films were also formed over the rest of the weldment, and this resulted in the similar current density values recorded across the surface of the weldment. However, this does not imply that corrosion is no longer taking place. In fact, for fully activated regions with the formation of corrosion products or film over the pit mouth, corrosion activities occur beneath the surface. Donatus and coworkers [29] have once reported that once localized corrosion activities propagate significantly below the top surface, such as the case of an intergranular attack spreading tens of microns beneath the surface, current density values (recorded by the SVET) over such an area are relatively within the same range of those of the adjacent regions. Nonetheless, it is clear that the SZ is the region that is most resistant to corrosion and the PM is the region that is most susceptible to corrosion in 0.1 mol L^{-1} NaCl solution, and this is evident from the early hours of exposure to this medium.

As already mentioned in Section 2, immersion tests were also conducted in other solutions: 3.5% NaCl solution; acidified 3.5% NaCl solution (A-3.5% NaCl solution); and EXCO solution. Micrographs of the different zones of the weldment obtained after 24 h of immersion in these solutions are presented in Figs. 10–12. Fig. 10 displays the optical and SEM micrographs of the SZ for the three solutions respectively. In all the solutions, the corrosion attacks in the SZ were not pronounced. This is because the active T_1 precipitates were totally dissolved, and the re-precipitated Cu-rich precipitates were uniformly spread across the SZ. In addition, the Cu-rich precipitates appear not to be as electrochemically active as the T_1 precipitates. The T_1 phase, with a corrosion potential of -1.096 ± 0.003 V (SCE) in aerated 0.6 M NaCl solution, is anodic to the α-Al matrix with a corrosion potential of -0.729 ± 0.002 V (SCE) [30]. It corrodes preferentially through initial leaching of its Al and Li components in a manner similar to how the Al and Mg components of the S (Al_2CuMg) phase are first dissolved. However, the corrosion morphologies or features were different from solution to solution. Strange filiform-like corrosion attacks were observed on the SZ of the weldment exposed to 3.5% NaCl solution (Fig. 10(a) and (b)). This form of attack was rarely found on the SZ of the weldment exposed to A-3.5% NaCl solution (Fig. 10(c)); only one similar attack was found as shown in Fig. 10(d). Generally, while multiple superficial pits were observed in the acidified solution, the filiform-like attacks were observed in the 3.5% NaCl solution. The filiform-like attacks were observed to be propagated along the direction of tool rotation. This suggests that the attacks may be associated with second phase particles clustered in this direction. However, traces of such type of attack were also found in the TMAZ, outside the tool domain. This implies that the occurrence of this type of attack may not be related to clusters of particles and may be due to clustering of atoms of active elements (such as Mg and Li) as a result of diffusion since these zones (SZ and TMAZ) experience the highest temperature during the welding process.

In the SZ of the weldment exposed to EXCO solution, an entirely different form of attack was revealed. The attack appeared to be associated with coarse second phase particles in the SZ. Clearly, the different forms of the attack revealed in all the solutions can be attributed to the variations in pH values and compositions, in addition to the suggested clustering (that was mentioned for the filiform-like form of attack observed in the 3.5% NaCl solution).

The case of the HAZ was somewhat different. Clear cases of intergranular corrosion were revealed both in the 3.5% NaCl solution (Fig. 11(a)–(b)) and in the EXCO (Fig. 11(c)–(d)). As revealed in Fig. 3, selective precipitation occurred at the grain boundaries of the TMAZ and HAZ during the welding process. This makes the GBs to be more active, compared with the adjacent matrix, with a consequent boundary dissolution when immersed in the media. In all, the attacks were somewhat superficial, but slightly more pronounced compared with that of the SZ.

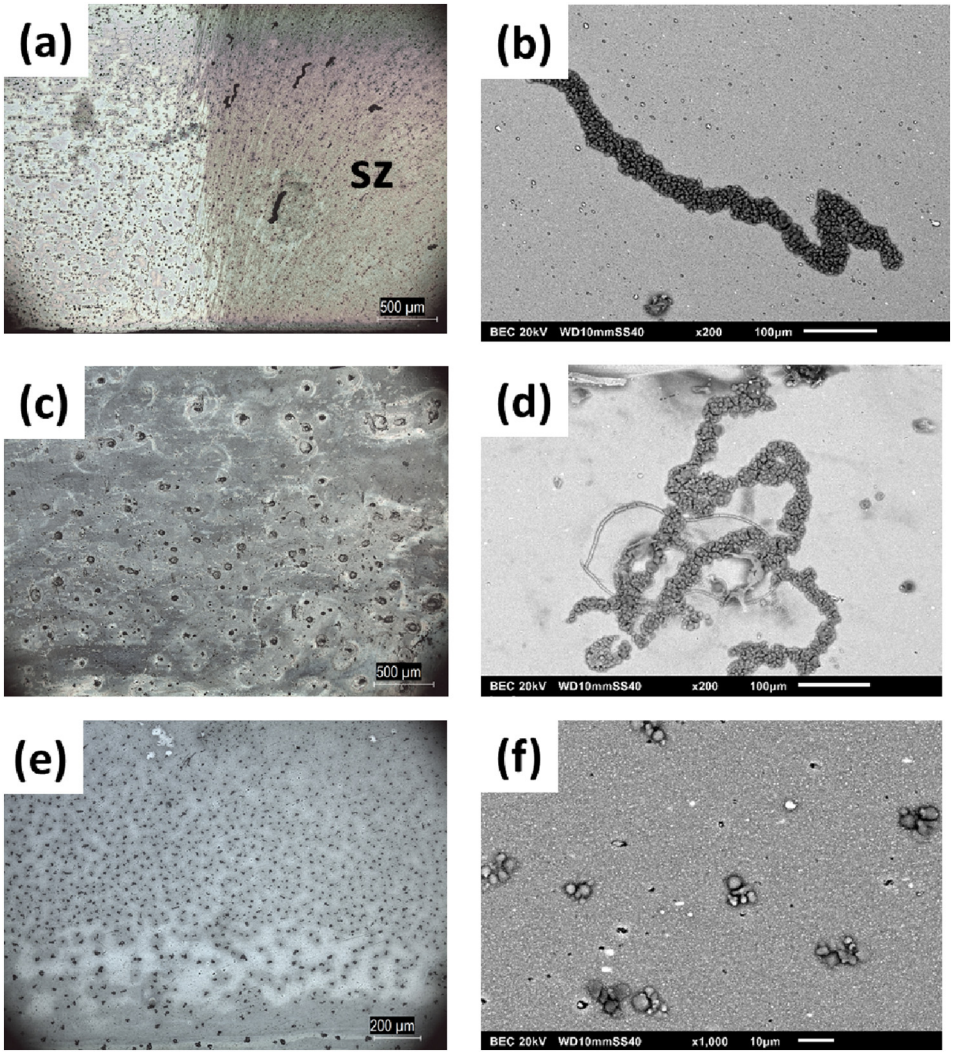

Fig. 10. Optical and SEM micrographs of the SZ surface of the AA2198-T851 friction stir weldment after 24 h immersion test in (a) & (b) 3.5% NaCl solution, (c) &(d) acidified 3.5% NaCl solution, and (e) & (f) EXCO solution. Panels (a), (c) and (e) are optical micrographs.

Displayed in Fig. 12 are the optical images of the surfaces exposed to the different media and their respective cross-sectional micrographs. Unlike in the SZ and HAZ, the corrosion attack in the PM was pronounced in all the solutions. While the PM in 3.5% NaCl solution corroded with a few large pits, the PM in the acidified solution corroded with multiple pits; and in the EXCO solution, the entire surface was corroded. Hydrogen evolution (indicated by arrows) was immense across the entire surface that was covered with a salt film (as revealed by the inset in Fig. 12(e)). The cross-sectional images show that the attack depths were nearly in the same range for the 3.5% NaCl solution and the acidified solution. The depth of attack in the EXCO solution was clearly far more than the depths in the other two solutions. Fig. 12(f) shows that the GBs were not susceptible as they were intact. The attack only propagated through the grains. The image also reveals that the attacks were intragranular and propagated crystallographically along preferred bands, with exfoliating surface layers in the direction of propagation. The crystallographic form of propagation [23,31] may be related to orientation dependent grain distinct layers as reported in the literature [32–34]. The T_1 phase is associated with the susceptibility in this region. Its volume fraction within the grain is high, as earlier revealed in Section 3.1. The fact that the GBs in this region are intact confirms that the TI precipitates may not be present at the GBs.

Thus, in order of corrosion susceptibility, the PM is the most susceptible, followed by the HAZ, and the TMAZ. The SZ is the region that is most resistant to corrosion. This follows the order of variations in the population density of the T_1 phase in these regions. Presented in Fig. 13(a)–(b) are open circuit potential (OCP) measurements of the SZ, HAZ and PM in A-3.5% NaCl solution (Fig. 13(a)) and in EXCO solution (Fig. 13(b)), respectively. In the A-3.5% NaCl solution, the measured potential for the SZ was the highest (in the range of −0.62 V), while those of the HAZ and PM were lower (between −0.65 V and −0.67 V). Also, in the EXCO solution, the measured potential for the SZ was the highest (between −0.63 V and − 0.65 V), while that of the PM was the lowest (between −0.68 V and −0.73 V). For the HAZ, the potential varied significantly. In some cases, the potential ranged between −0.64 V and −0.68 V as exemplified by the curve labelled HAZ-I in Fig. 13(b); and in other cases in ranged between −0.68 V and −0.72 V (about the same range as that of the PM) as exemplified by the curve labelled HAZ-II in Fig. 13(b). However, the OCP values for the HAZ were always between those of the SZ and those of the PM. They were never lower than those of the PM. The implication of this is that in agreement with the SVET data and microstructural observations, the

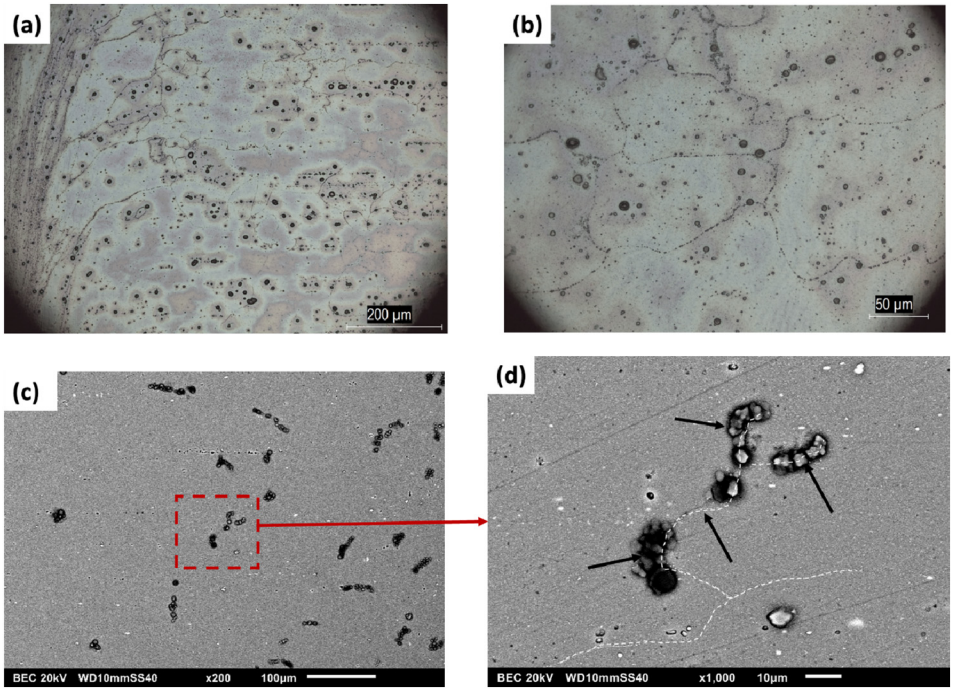

Fig. 11. (a)–(b) Optical micrographs of the surface of the HAZ and adjacent TMAZ of the AA2198-T851 friction stir weldment after 24 h immersion test in 3.5% NaCl solution. (c)–(d) SEM micrographs of the TMAZ surface of the AA2198-T851 friction stir weldment after 24 h immersion test in EXCO solution.

OCP results show that the SZ exhibited the least tendency to corrode in both solutions, while the PM exhibited the highest tendency to corrode. The HAZ exhibited more tendency compared with the SZ but lesser or equal tendency compared with the PM. These results also agree with the maximum depths of attack in the various zones after 24 h exposure to EXCO solution (Fig. 13(c)–(e)). The measured maximum depths of the attack were: 20 μm in the SZ; 27 μm in the TMAZ/HAZ region; 98 μm in the HAZ adjacent to the PM; and 119 μm in the PM. This further confirms that the extent of corrosion susceptibility is in the order PM > HAZ/TMAZ > SZ. Additionally, it is also evident from the cross-sectional images (Fig. 13(c)–(e)) that the forms of attack in the SZ and the TMAZ/HAZ region are different from that of the PM.

Given that the SZ is most noble compared with the other zones, with the PM being the most active of all the zones, it is not out of place to suggest that galvanic interactions occurred during the immersion tests. This is supported by the fact that the microstructural examinations revealed that the SZ and the adjacent HAZ were minimally corroded in the aggressive media employed compared with the most active PM. In essence, the attacks on the PM were more pronounced because there were coupled cathodic regions (the SZ, TMAZ and HAZ) to sustain the localized anodic activities on the PM.

So far, there is a clear relationship between the corrosion susceptibility of the AA2198-T851 friction stir weldment with microhardness, and this is governed majorly by the variation of the density of T_1 precipitates in the individual zones.

3.3. Anodic Hydrogen Evolution

Hydrogen evolution was observed to be intense on the PM side of the AA2198-T851 weldment, especially in the most aggressive EXCO solution. Presented in Fig. 14(a)–(b) are the successive images of the cross-section of the PM after 24 h immersion test in EXCO solution. Surprisingly, corrosion products and hydrogen bubbles were observed coming out in significant proportions from the corrosion fronts at the cross-section of the PM as the attack penetrated the alloy, as evident from the micrographs. The interesting part is that the images were obtained approximately 15 h after the immersion test. Immediately after the immersion test, the samples were thoroughly rinsed in deionised water and left in a cool air stream to dry for up to an hour. After 13 h, the samples were embedded in a resin and sequentially polished to 1 μm surface finish, dried and air cooled for several minutes before micro-examination.

After about 2 days, the products had solidified as shown in the SEM micrographs of Fig. 14(c)–(d). EDS analysis reveals that these products were high in chloride concentration. This was not observed in the other regions of the weldment nor was it observed in other solutions; indicating that the PM is highly susceptible to corrosion. Fig. 14(d) further confirms that the attack is intragranular and the corrosion pathway [32] is crystallographic propagating through the grains. However, the main point is that copious amounts of hydrogen bubbles were evolved from the severe localized corrosion sites of the PM (AA2198-T851 Al) at its free corrosion potential. This is because of its high corrosion susceptibility due to the presence of high volume fraction of the T_1 precipitates.

For Al alloys, hydrogen evolution does not only occur at the free corrosion potential, it also occurs when the alloys are polarized anodically [21,22,35–38]. This phenomenon is often referred to as the negative difference effect (NDE) or anodic hydrogen evolution (AHE). AHE is observed in other alloys with Mg being the most researched, and the subject of AHE is under debate [39,40]. Nevertheless, in our recently published work [41], we have been able to show that it is possible to use the anodic hydrogen evolution effect to qualitative assess the corrosion behaviour of AA2198-T851 alloy, by using a cell designed to expose a surface area of 0.025 cm^2. By using this cell, current spikes can be observed at the anodic arm of potentiodynamic polarization curves of Al alloys. The current spikes are associated with repetitive

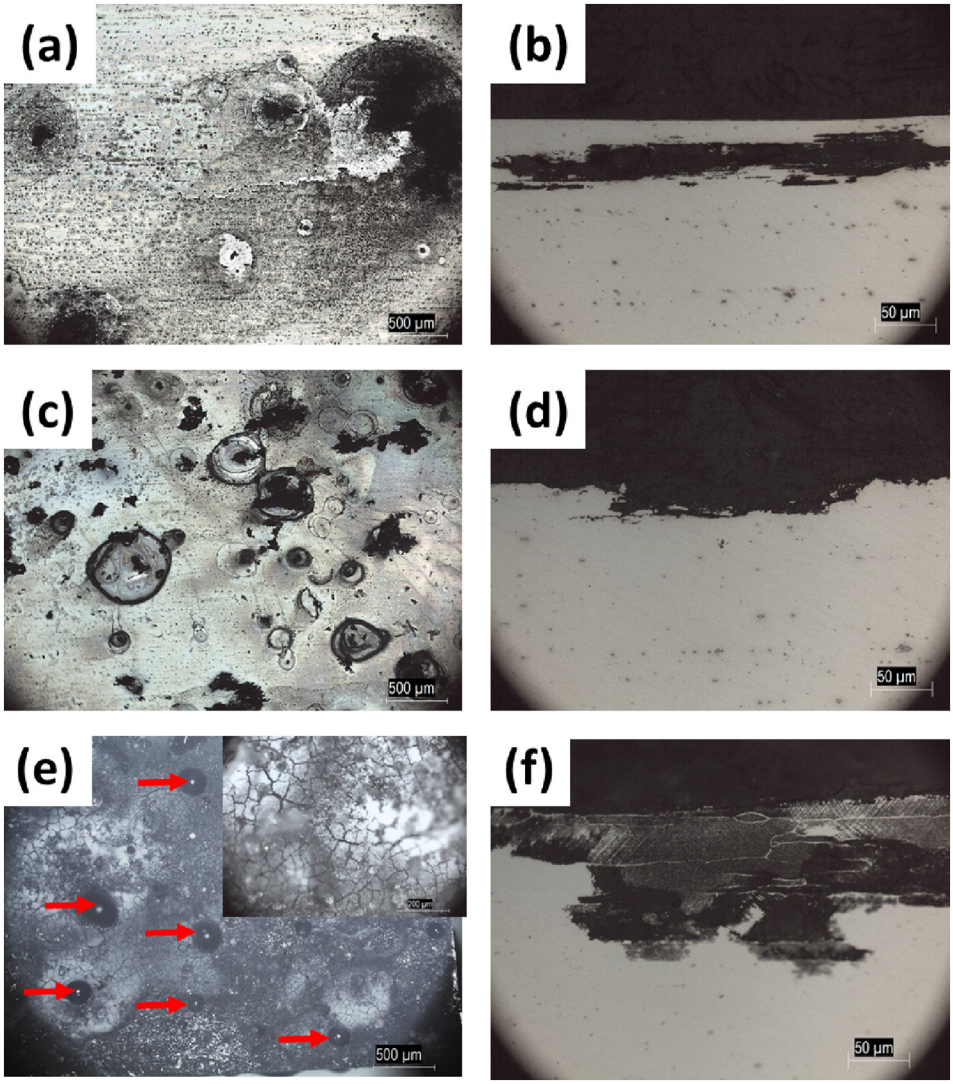

Fig. 12. Surface and cross-sectional optical micrographs of the PM of the AA2198-T851 friction stir weldment after 24 h immersion test in (a) & (b) 3.5% NaCl solution, (c) & (d) acidified 3.5% NaCl solution, and (e) & (f) EXCO solution.

bubble formation, coalescence, and detachment from the pit mouth. Coalescence at the pit mouth leads to reduction in measured current density values, while detachment leads to current density spikes. Furthermore, it was also revealed that the spikes became pronounced after a critical potential. This potential is associated with the addition of the dissolution of enriched Cu (at the surface of the alloy) to the on-going dissolution of Al. The method was used to show that the PM of the AA2198-T851 weldment generated more hydrogen bubbles compared with the SZ. Current density spikes were not observed in the cathodic arm possibly because the predominant reduction reaction, in the potential range considered, was the one involving H^+ ions and O_2 as reactants and H_2O as the product (i.e. $4H^+ + O_2 + 4e^- = 2H_2O$). On the other hand, during anodic polarization, H^+ ions were produced from hydrolysis of Al^{3+} ions at the corrosion front. The H^+ ions produced were subsequently reduced to H_2 bubbles at the walls of the pits or at the mouths of the pits, which were more cathodic compared with the active corrosion front. These bubbles coalesced to form larger bubbles at the mouths of the pits. The coalescence and release of the bubbles from the surface of the alloy resulted in the formation of current density spikes during anodic polarization [41].

In this work, the HAZ of the weldment was included in the analysis. Presented in Fig. 15 are the potentiodynamic polarization curves obtained in A-3.5% NaCl solution and EXCO solution for the PM (a), HAZ (b), and SZ (c). The curves obtained in the A-3.5% NaCl solution, compared with the EXCO solution, showed lower corrosion rates in all the zones. Current density spikes were observed in all the curves in both solutions. However, the spikes were more pronounced in the EXCO solution due to more hydrogen bubble evolution. Interestingly, a decrease in the intensity of the current density spikes was observed from zone to zone. The PM exhibited the highest intensity of spikes, especially above −0.3 V, followed by the HAZ; and the least intensity of current density spikes was observed in the SZ.

As mentioned earlier, because the T_1 precipitates dissolve and their volume fraction reduces continuously as the SZ is approached, the corrosion resistance of the weldment increases from the PM to the TMAZ, and it is highest at the SZ. Correspondingly, the volume of hydrogen bubbles evolved decreased from the PM to the SZ.

In all, the T_1 precipitates are responsible for impediment to

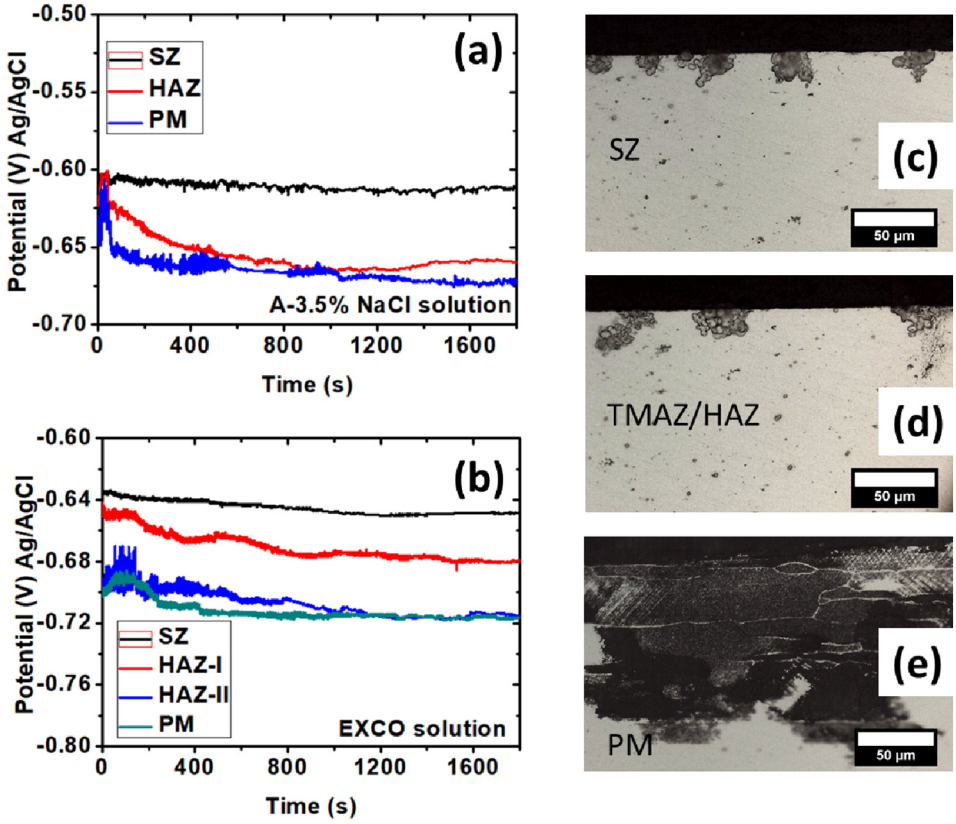

Fig. 13. (a)–(b) OCP measurements of the SZ, HAZ and PM in (a) A-3.5% NaCl solution and (b) EXCO solution. (c)–(e) Optical micrographs showing the depths of attack in the weld regions of the AA2198-T851 friction stir weldment after 24 h exposure to EXCO solution.

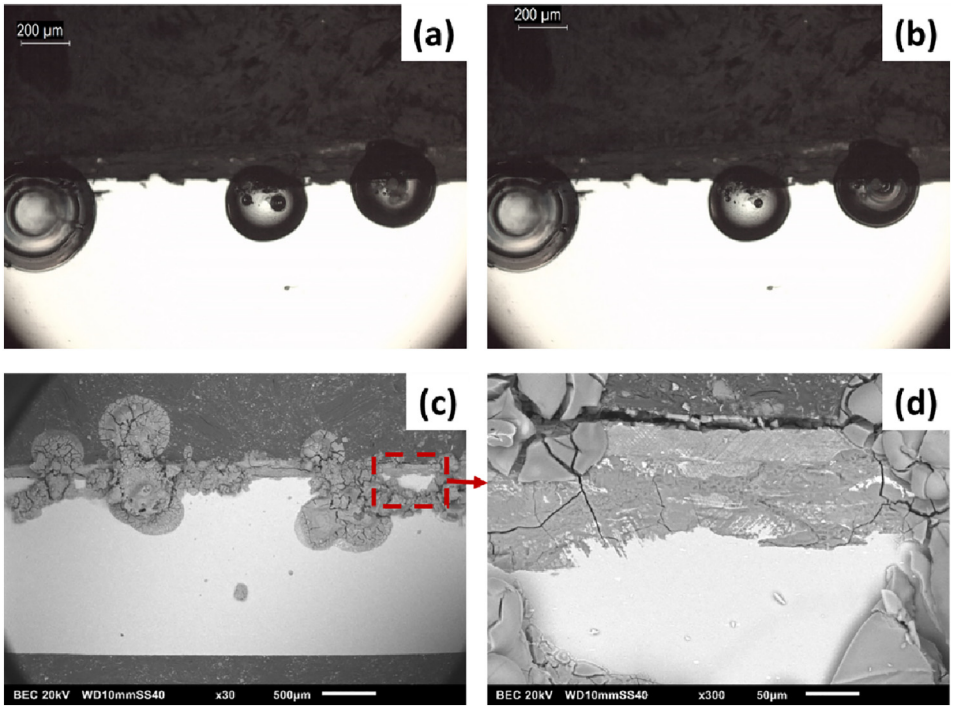

Fig. 14. (a)–(b) Cross-sectional optical micrographs of the PM of the AA2198-T851 friction stir weldment obtained in rapid succession showing in-situ hydrogen evolution and generation of liquid corrosion product. (c)–(d) SEM micrographs showing the corrosion products after solidification and corrosion morphology.

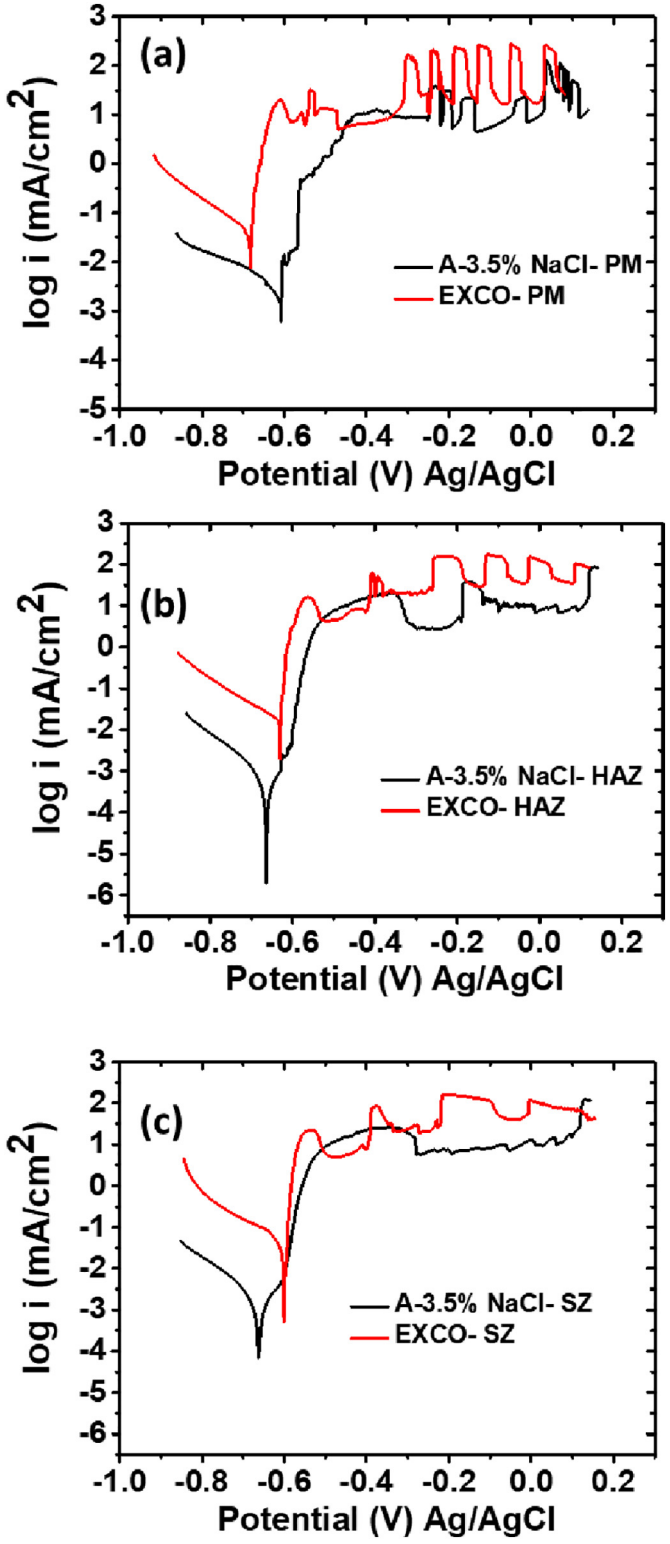

Fig. 15. Potentiodynamic polarization curves of the (a) PM, (b) HAZ and (c) SZ of the AA2198-T851 friction stir weldment obtained in acidified 3.5% NaCl solution and EXCO solution.

dislocation movement and are also responsible for corrosion susceptibility. Because they are far more active compared with the matrix [30], in an enabling environment, galvanic cells created between the T_1 precipitates and the adjacent matrix enhances the rapid dissolution of the T_1 precipitates. The T_1 phase dissolves by losing its Al and Li components, leaving behind a Cu rich remnant. With time as the matrix is further dissolved, Cu is released into the electrolyte. Away from the bulk, the released Cu attains its free corrosion potential and becomes ionised. The formed Cu ions are later re-deposited at micro-cathodic sites. The Al ions formed from the dissolution of the active phases and the matrix reacts with H_2O to produce H^+ ions, which combine by accepting electrons to produce H_2 bubbles.

Thus, the T_1 phase links the microhardness variations with the corrosion resistance and volume of anodic hydrogen bubbles evolved during dissolution in all the zones of the weldment. The higher the density of the T_1 precipitates the higher the hardness, the lower the corrosion resistance and the higher the volume of hydrogen bubbles evolved during corrosion. Therefore, for an AA2198-T851 friction stir weldment, it can be concluded that the microhardness in the weld zones has an inverse relationship with the corrosion resistance, and a direct relationship with the volume of hydrogen bubbles evolved during corrosion. Presented in Fig. 16 is a combination of images and plot summarising the relationship between corrosion resistance, hydrogen evolution, microhardness and the population density of the T_1 particles. The bullet points below explain this figure.

- **PM** [highest volume fraction of T_1 precipitates → highest microhardness; lowest corrosion resistance (or highest corrosion susceptibility); highest hydrogen bubble evolution].
- **HAZ** [decreased volume fraction of T_1 precipitates relative to PM → decreased microhardness; increased corrosion resistance (or decreased corrosion susceptibility); decreased hydrogen bubble evolution].
- **TMAZ** [further decreased volume fraction of T_1 precipitates relative to PM → further decreased microhardness; further increased corrosion resistance (or decreased corrosion susceptibility); further decreased hydrogen bubble evolution].
- **SZ** [lowest volume fraction of T_1 precipitates → lowest microhardness; highest corrosion resistance (or lowest corrosion susceptibility); lowest hydrogen bubble evolution].

4. Conclusions

The correlation between corrosion resistance, microhardness and hydrogen evolution in the friction stir weldment of AA2198-T851 has been studied and the following conclusions are drawn.

1. The parent material contains different variants of precipitates including composites precipitates. However, the T_1 phase was the most predominant phase. The HAZ contained less volume fraction of the T_1 phase compared with the PM since coarsening and partial dissolution of the precipitates occurred in the HAZ as a result of the high temperature experienced in this zone. In the SZ, the T_1 particles were almost completely dissolved, and the predominant nano-sized dispersoids and clustered δ′/β′ shaped particles.
2. Cu-rich precipitates, different from the T_1 phase, were re-precipitated uniformly in the SZ but re-precipitated at the grain boundaries of the TMAZ and HAZ. The population density of the Cu-rich precipitates increased as the SZ was approached while that of the T_1 precipitates decreased correspondingly.
3. Highest microhardness values were recorded in the PM due to the highest volume fraction of the T_1 precipitates present in this region, but the corrosion resistance was the least compared with other zones. The microhardness values gradually reduced in the HAZ as the volume fraction of the T_1 phase decreased. Low microhardness values were recorded in the SZ due to the almost complete dissolution of the T_1 precipitates. Correspondingly, the corrosion resistance also increased from the PM to the SZ, with the SZ showing

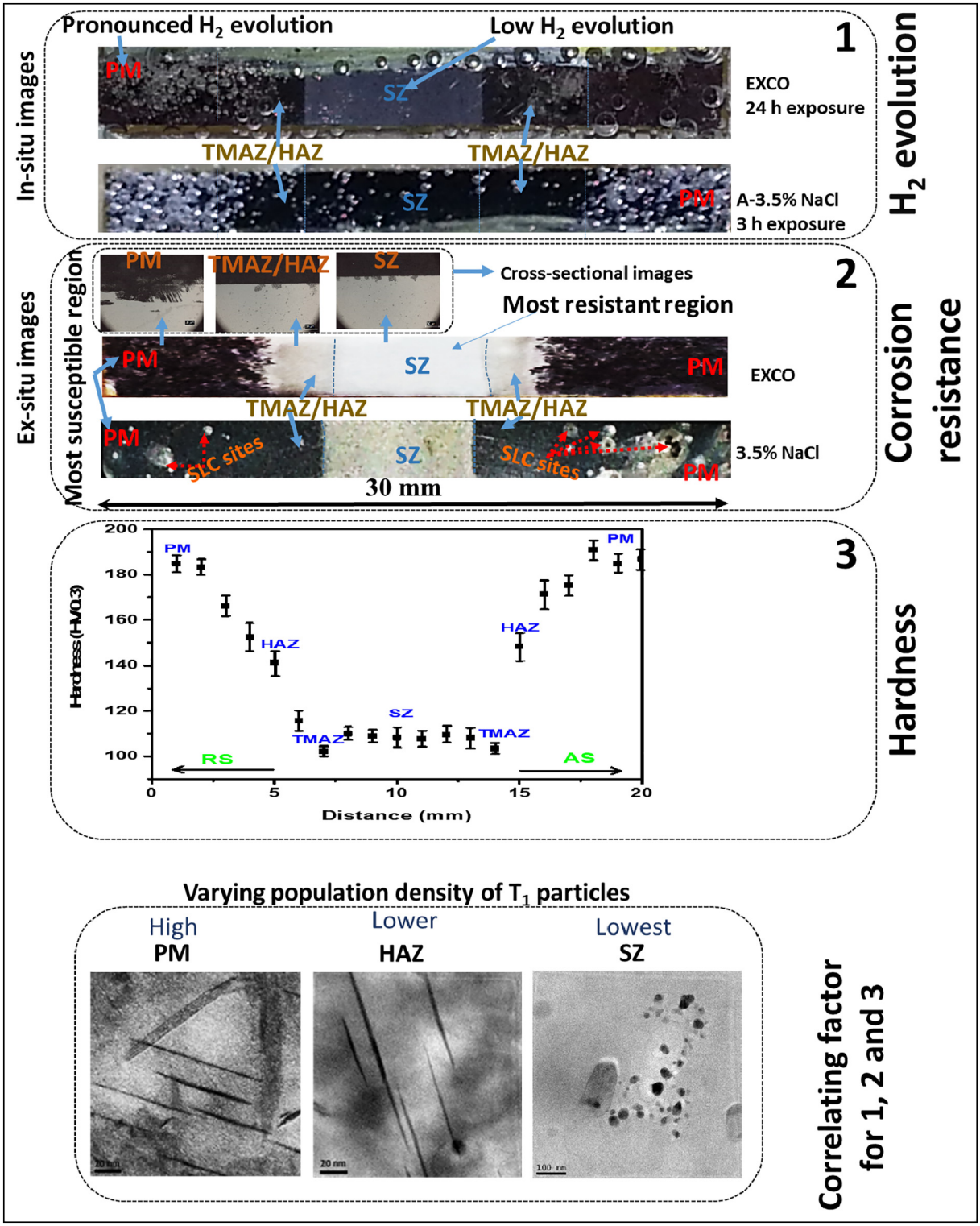

Fig. 16. Merged images and plot summarising the correlation between microhardness, corrosion resistance, hydrogen evolution and population density of T_1 particles.

the highest resistance to corrosion. Expectedly, the changes in corrosion resistance were inversely related to anodic hydrogen evolution.

4. A strong correlation exists between the microhardness, corrosion resistance and anodic hydrogen evolution during dissolution since they are all dependent on the volume fraction of T_1 phase across the friction stir weldment of the alloy.
5. The forms of corrosion revealed in the SZ were different for different solutions. Filiform-like attack was observed in 3.5% NaCl solution, whereas attacks associated with coarse intermetallic particles were observed in EXCO solution. However, the form of corrosion was the same in the PM. The attack was intragranular but propagated crystallographically.

Acknowledgement

The authors would like to thank FAPESP for financial support (Proc. 2013/13235-6) and for the sponsorship of the postdoctoral fellowship of Dr. Uyime Donatus (Proc.2017/03095-3). Acknowledgements are also due to CCTM/IPEN for the facilities provided, especially for TEM analysis (Nildemar Aparecido M. Ferreira) and to EPUSP-Mechatronics Department for SEM analysis (Dr. Izabel Fernanda Machado).

Data Availability Statement

The raw/processed data required to reproduce these findings cannot be shared at this time as the data also forms part of an ongoing study.

References

[1] T. Dursun, C. Soutis, Recent developments in advanced aircraft aluminium alloys, Mater. Des. 56 (2014) 862–871, https://doi.org/10.1016/j.matdes.2013.12.002.
[2] R.J. Rioja, J. Liu, The evolution of Al-Li base products for aerospace and space applications, Metall. Mater. Trans. A Phys. Metall. Mater. Sci. 43 (2012) 3325–3337, https://doi.org/10.1007/s11661-012-1155-z.
[3] P.L. Threadgill, A.J. Leonard, H.R. Shercliff, P.J. Withers, Friction stir welding of aluminium alloys, Int. Mater. Rev. 54 (2009) 49–93, https://doi.org/10.1179/174328009X411136.
[4] R.W. Fonda, J.F. Bingert, Precipitation and grain refinement in a 2195 Al friction stir weld, Metall. Mater. Trans. A Phys. Metall. Mater. Sci. 37 (2006) 3593–3604, https://doi.org/10.1007/s11661-006-1054-2.
[5] M. Jariyaboon, A.J. Davenport, R. Ambat, B.J. Connolly, S.W. Williams, D.A. Price, The effect of welding parameters on the corrosion behaviour of friction stir welded AA2024-T351, Corros. Sci. 49 (2007) 877–909.
[6] R.S. Mishra, Z.Y. Ma, Friction stir welding and processing, Mater. Sci. Eng. R. Rep. 50 (2005) 1–78, https://doi.org/10.1016/j.mser.2005.07.001.
[7] H. Sidhar, R.S. Mishra, Aging kinetics of friction stir welded Al-Cu-Li-Mg-Ag and Al-Cu-Li-Mg alloys, Mater. Des. 110 (2016) 60–71, https://doi.org/10.1016/j.matdes.2016.07.126.
[8] Y. Deng, R. Ye, G. Xu, J. Yang, Q. Pan, B. Peng, X. Cao, Y. Duan, Y. Wang, L. Lu, Z. Yin, Corrosion behaviour and mechanism of new aerospace Al–Zn–Mg alloy friction stir welded joints and the effects of secondary Al3ScxZr1 − x nanoparticles, Corros. Sci. (2014), https://doi.org/10.1016/j.corsci.2014.10.036.
[9] U. Donatus, G.E. Thompson, X. Zhou, J. Wang, K. Beamish, Flow patterns in friction stir welds of AA5083 and AA6082 alloys, Mater. Des. 83 (2015) 203–213, https://doi.org/10.1016/j.matdes.2015.06.006.
[10] M. Esmaily, N. Mortazavi, W. Osikowicz, H. Hindsefelt, J.E. Svensson, M. Halvarsson, G.E. Thompson, L.G. Johansson, Corrosion behaviour of friction stir-welded AA6005-T6 using a bobbin tool, Eval. Program Plann. 111 (2016) 98–109, https://doi.org/10.1016/j.corsci.2016.04.046.
[11] M. Esmaily, J.E. Svensson, L.G. Johansson, Technical Note: A Major Loss in Tensile Strength of Friction Stir Welded Aluminum Alloy Joints Resulting From Atmospheric Corrosion, 72 (2016), pp. 1587–1596.
[12] M. Esmaily, Z. Mortazavi, C. Osikowicz, C.E. Hindsefelt, M. Svensson, B.E. Halvarsson, A.G. Johanssona Thompson, Influence of multi-pass friction stir processing on the corrosion behavior of an Al-Mg-SiAlloy, J. Electrochem. Soc. 163 (2016) 124–130, https://doi.org/10.1149/2.1091603jes.
[13] X. Zhang, B. Liu, X. Zhou, J. Wang, C. Luo, Z. Sun, Z. Tang, F. Lu, Corrosion behavior of friction stir welded 2A97 Al-Cu-Li alloy, Corrosion 9312 (2017) 2418, , https://doi.org/10.5006/2418.
[14] E. Bousquet, A. Poulon-Quintin, M. Puiggali, O. Devos, M. Touzet, Relationship between microstructure, microhardness and corrosion sensitivity of an AA 2024-T3 friction stir welded joint, Corros. Sci. 53 (2011) 3026–3034, https://doi.org/10.1016/j.corsci.2011.05.049.
[15] D.A. Wadeson, X. Zhou, G.E. Thompson, P. Skeldon, L.D. Oosterkamp, G. Scamans, Corrosion behaviour of friction stir welded AA7108 T79 aluminium alloy, Corros. Sci. 48 (2006) 887–897, https://doi.org/10.1016/j.corsci.2005.02.020.
[16] V. Proton, J. Alexis, E. Andrieu, J. Delfosse, A. Deschamps, F. De Geuser, M.C. Lafont, C. Blanc, The influence of artificial ageing on the corrosion behaviour of a 2050 aluminium-copper-lithium alloy, Corros. Sci. 80 (2014) 494–502, https://doi.org/10.1016/j.corsci.2013.11.060.
[17] U. Donatus, G.E. Thompson, X. Zhou, Anodizing behavior of friction stir welded dissimilar aluminum alloys, J. Electrochem. Soc. 162 (2015) C657–C665, https://doi.org/10.1149/2.0651512jes.
[18] U. Donatus, G.E. Thompson, X. Zhou, Effect of prior sputter deposition of pure aluminium on the corrosion behaviour of anodized friction stir weld of dissimilar aluminium alloys, 123 SMM, 2016, pp. 126–129, https://doi.org/10.1016/j.scriptamat.2016.06.015.
[19] V. Proton, J. Alexis, E. Andrieu, J. Delfosse, M.-C. Lafont, C. Blanc, Characterisation and understanding of the corrosion behaviour of the nugget in a 2050 aluminium alloy Friction Stir Welding joint, Corros. Sci. 73 (2013) 130–142, https://doi.org/10.1016/j.corsci.2013.04.001.
[20] V. Proton, J. Alexis, E. Andrieu, C. Blanc, J. Delfosse, L. Lacroix, G. Odemer, Influence of post-welding heat treatment on the corrosion behavior of a 2050-T3 aluminum-copper-lithium alloy friction stir welding joint, J. Electrochem. Soc. 158 (2011) C139–C147, https://doi.org/10.1149/1.3562206.
[21] M. Curioni, F. Scenini, The mechanism of hydrogen evolution during anodic polarization of Aluminium, Electrochim. Acta 180 (2015) 712–721, https://doi.org/10.1016/j.electacta.2015.08.076.
[22] G.S. Frankel, S. Fajardo, B.M. Lynch, Introductory lecture on corrosion chemistry: a focus on anodic hydrogen evolution on Al and Mg, Faraday Discuss. 180 (2015) 11–33, https://doi.org/10.1039/C5FD00066A.
[23] U. Donatus, M. Terada, C.R. Ospina, F.M. Queiroz, A. Fatima Santos, I. Costa Bugarin, On the AA2198-T851 alloy microstructure and its correlation with localized corrosion behaviour, Corros. Sci. 131 (2018) 300–309, https://doi.org/10.1016/j.corsci.2017.12.001.
[24] D.L. Chen, M.C. Chaturvedi, Effects of welding and weld heat-affected zone simulation on the microstructure and mechanical behavior of a 2195 aluminum-lithium alloy, Metall. Mater. Trans. A Phys. Metall. Mater. Sci. 32 (2001) 2729–2741, https://doi.org/10.1007/s11661-001-1025-6.
[25] L.A.H. Terrones, S.N. Monteiro, Composite precipitates in a commercial Al-Li-Cu-Mg-Zr alloy, Mater. Charact. 58 (2007) 156–161, https://doi.org/10.1016/j.matchar.2006.04.008.
[26] F. De Geuser, B. Malard, A. Deschamps, Microstructure mapping of a friction stir welded AA2050 Al-Li-Cu in the T8 state, Philos. Mag. 94 (2014) 1451–1462, https://doi.org/10.1080/14786435.2014.887862.
[27] A.K. Shukla, W.A. Baeslack, Study of process/structure/property relationships in friction stir welded thin sheet Al–Cu–Li alloy, Sci. Technol. Weld. Join. 14 (2009) 376–387, https://doi.org/10.1179/136217109X412409.
[28] C. Gao, Z. Zhu, J. Han, H. Li, Correlation of microstructure and mechanical properties in friction stir welded 2198-T8 Al-Li alloy, Mater. Sci. Eng. A 639 (2015) 489–499, https://doi.org/10.1016/j.msea.2015.05.038.
[29] U. Donatus, G.E. Thompson, H. Liu, D. Elabar, Analyses of the sequential stages of corrosion on AA2024T3 using the scanning vibrating electrode technique (SVET), J. Mater. Eng. Perform. 24 (2015) 3808–3814, https://doi.org/10.1007/s11665-015-1701-0.
[30] R.G. Buchheit, J.P. Moran, G.E. Stoner, Electrochemical behavior of the T1 (Al2CuLi) intermetallic compound and its role in localized corrosion of Al-2%Li-3%Cu alloys, Corrosion 50 (1994) 120–130, https://doi.org/10.5006/1.3293500.
[31] X. Zhang, X. Zhou, T. Hashimoto, B. Liu, C. Luo, Z. Sun, Z. Tang, F. Lu, Y. Ma, Corrosion behaviour of 2A97-T6 Al-Cu-Li alloy: the influence of non-uniform precipitation, Corros. Sci. 132 (2018) 1–8, https://doi.org/10.1016/j.corsci.2017.12.010.
[32] U. Donatus, G.E. Thompson, J.A. Omotoyinbo, K.K. Alaneme, S. Aribo, O.G. Agbabiaka, Corrosion pathways in aluminium alloys, Trans. Nonferrous Metals Soc. China 27 (2017) 55–62, https://doi.org/10.1016/S1003-6326(17)60006-2.
[33] U. Donatus, G.E. Thompson, D. Elabar, T. Hashimoto, S. Morsch, Features in aluminium alloy grains and their effects on anodizing and corrosion, Surf. Coat. Technol. 277 (2015) 91–98, https://doi.org/10.1016/j.surfcoat.2015.07.034.
[34] U. Donatus, G.E. Thompson, X. Zhou, J. Alias, I.-L.L. Tsai, Grain distinct stratified nanolayers in aluminium alloys, Mater. Chem. Phys. 188 (2017) 109–114, https://doi.org/10.1016/j.matchemphys.2016.12.021.
[35] D.M. Dražić, J. Popić, Hydrogen evolution on aluminium in chloride solutions, J. Electroanal. Chem. 357 (1993) 105–116, https://doi.org/10.1016/0022-0728(93)80377-T.
[36] C. Laurent, F. Scenini, T. Monetta, F. Bellucci, M. Curioni, The contribution of hydrogen evolution processes during corrosion of aluminium and aluminium alloys investigated by potentiodynamic polarisation coupled with real-time hydrogen measurement, Npj Mater. Degrad. 1 (2017) 6, , https://doi.org/10.1038/s41529-017-0011-4.
[37] D.M. Drazic, J.P. Popic, Corrosion rates and negative difference effects for Al and some Al alloys, J. Appl. Electrochem. 29 (1999) 43–50.
[38] A.R. Despić, J. Radošević, P. Dabić, M. Kliškić, Abnormal yields of hydrogen and the mechanism of its evolution during cathodic polarization of aluminium, Electrochim. Acta 35 (1990) 1743–1746, https://doi.org/10.1016/0013-4686(90)87074-C.
[39] S. Thomas, N.V. Medhekar, G.S. Frankel, N. Birbilis, Corrosion mechanism and hydrogen evolution on mg, Curr. Opin. Solid State Mater. Sci. 19 (2015) 85–94, https://doi.org/10.1016/j.cossms.2014.09.005.
[40] M. Esmaily, J.E. Svensson, S. Fajardo, N. Birbilis, G.S. Frankel, S. Virtanen, R. Arrabal, S. Thomas, L.G. Johansson, Progress in Materials Science Fundamentals and advances in magnesium alloy corrosion, Prog. Mater. Sci. 89 (2017) 92–193, https://doi.org/10.1016/j.pmatsci.2017.04.011.
[41] U. Donatus, L.O. Berbel, I. Costa, Qualitative use of potentiodynamic polarization and anodic hydrogen evolution in the assessment of corrosion susceptibility in AA2198-T851 Al-Cu-Li alloy, Mater. Corros. (2018) 1–14, https://doi.org/10.1002/maco.201810108.